



Nanoscale magnetic field imaging for 2D materials

Estefani Marchiori¹, Lorenzo Ceccarelli¹, Nicola Rossi¹, Luca Lorenzelli²,
Christian L. Degen^{1,3} and Martino Poggio^{1,3}✉

Abstract | Nanoscale magnetic imaging can provide microscopic information about length scales, inhomogeneity and interactions of materials systems. As such, it is a powerful tool to probe phenomena such as superconductivity, Mott insulating states and magnetically ordered states in 2D materials, which are sensitive to the local environment. This Technical Review provides an analysis of weak magnetic field imaging techniques that are most promising for the study of 2D materials: magnetic force microscopy, scanning superconducting quantum interference device microscopy and scanning nitrogen-vacancy centre microscopy.

Magnetic imaging techniques provide invaluable insights into material properties that are not accessible through optical or topographic images. They shed light on magnetization patterns, spin configurations and current distributions. Unlike bulk measurements of transport, magnetization, susceptibility or heat capacity, magnetic imaging can provide microscopic information about length scales, inhomogeneity and interactions. In the last few decades, the development of magnetic imaging technologies has been driven by applications in magnetic storage and information processing. The need to understand magnetostatics and dynamics on the nanometre-scale and with high temporal resolution has led to powerful optical, electron, X-ray and scanning probe microscopies. There are a number of excellent reviews on these techniques and their myriad applications^{1–6}.

The confluence of substantial improvements in nanometre-scale magnetic imaging with the advent of engineered 2D materials creates the perfect opportunity to gain new insight into the physics of correlated states in condensed matter. The unprecedented control provided by layer-by-layer materials engineering gives us the opportunity to test theories on superconductivity, magnetism and other correlated phenomena. With this control, however, comes sensitivity to disorder and inhomogeneity. In such a fragile environment, local measurements — with sensors whose characteristic size is smaller than the length scale of the disorder — are essential for making sense of the system. Nanoscale magnetic imaging techniques can be used to image magnetization configurations and charge transport, giving crucial local information on quantum phases, including on the spatial variation of order parameters, the presence of domains and the role of defects.

A number of scanning probe microscopy (SPM) techniques have emerged as important tools for the

investigation of 2D systems. These include atomic force microscopy, scanning single-electron transistors^{7,8}, scanning gate microscopy⁹, scanning microwave impedance microscopy¹⁰, scanning tunnelling microscopy¹¹ and scanning near-field optical microscopy¹². Of interest here are the SPMs designed to map subtle magnetic field patterns non-invasively. Scanning superconducting quantum interference device (SQUID) microscopy (SSM) has been used to map superconducting currents¹³ and magnetization¹⁴ in magic-angle twisted bilayer graphene or quantum Hall edge channels in monolayer graphene^{15,16}. Scanning nitrogen-vacancy (NV) centre microscopy (SNVM) has been used to image layer-dependent magnetization in Cr-based van der Waals (vdW) magnets^{17–19}, as well as hydrodynamic electron flow in graphene^{20,21} and WTe₂ (REF.²²).

In this Technical Review, we discuss the most promising weak magnetic field imaging techniques for 2D materials: magnetic force microscopy (MFM), SSM and SNVM. We compare the capabilities of these techniques, their required operating conditions and assess their suitability to different types of source contrast, in particular, magnetization and current density. Finally, we focus on the prospects for improving each technique and speculate on its potential impact, especially in the rapidly growing field of 2D materials.

Imaging magnetization and current

Mapping magnetization patterns is important for investigations of magnetic domains, antiferromagnetism, magnetic skyrmion phases and the spin Hall effect. Measurements directly sensitive to magnetization include synchrotron-based X-ray techniques, neutron diffraction and electron polarization techniques. However, as 2D systems tend to have a tiny total magnetic moment, these techniques are usually not sensitive enough.

¹Department of Physics, University of Basel, Basel, Switzerland.

²Department of Physics, ETH Zürich, Zürich, Switzerland.

³Swiss Nanoscience Institute, University of Basel, Basel, Switzerland.

✉e-mail: martino.poggio@unibas.ch

<https://doi.org/10.1038/s42254-021-00380-9>

Key points

- Scanning magnetic probes have developed into powerful techniques for imaging magnetization patterns, spin configurations and current distributions with high spatial resolution and high sensitivity.
- These local probes give crucial insights into length scales, inhomogeneity and interactions that are often absent from bulk measurements of transport, magnetization, susceptibility or heat capacity.
- Using these techniques to image the recently discovered correlated states hosted in 2D materials will provide crucial local information on quantum phases, including on the spatial variation of order parameters, the presence of domains and the role of defects.
- Correlated states in 2D systems are extremely sensitive to disorder and inhomogeneity. In such a fragile environment, local measurements — with sensors whose characteristic size is smaller than the length scale of the disorder — are essential for making sense of the system.
- It is important to choose the appropriate scanning magnetic probe for the physical system under investigation: the different scaling of magnetization and current contrast with probe–sample spacing and the different physical quantities that are measured by each probe make certain techniques more amenable to certain systems.

Particularly sensitive techniques such as magneto-optic microscopy and spin-polarized scanning tunnelling microscopy have been used to reveal layer-dependent magnetism in flakes of CrI_3 (REF.²³) and films of CrBr_3 , grown by molecular beam epitaxy²⁴, respectively. However, the spatial resolution of magneto-optical techniques is limited to the micrometre-scale and interference effects can obscure magnetic signals in thin samples. Furthermore, spin-polarized scanning tunnelling microscopy requires atomically clean conducting surfaces, which can often only be obtained by thermal annealing. Because many magnetic vdW materials are volatile at high temperatures, this step is sometimes not possible. Magnetic imaging via the magnetic circular dichroism of X-ray photoemission electron microscopy has recently been applied to the vdW magnet Fe_3GeTe_2 (REFS^{25,26}). For a recent survey on the application of magnetization-sensitive techniques to 2D materials and especially to 2D magnets, we refer readers to REF.²⁷.

Here, we consider techniques capable of mapping magnetic stray field, because they are applicable to a wider set of phenomena than direct magnetization imaging. Stray fields are produced not only by magnetization patterns but also by current distributions. Transport imaging can be used to visualize local disorder, bulk and edge effects, electron guiding and lensing, topological currents, viscous electron flow, microscopic Meissner currents, and the flow and pinning of superconducting vortices. Common methods of mapping fields include the use of fine magnetic powders, as demonstrated by Bitter, Lorentz microscopy, electron holography and a number of SPM techniques. Those most applicable to 2D systems, for their combination of high spatial resolution and high magnetic field sensitivity, are MFM, SSM and SNVM (FIG. 1).

In general, a map of magnetic field cannot be reconstructed into a map of the source current or magnetization distribution. However, under certain boundary conditions, the source can be uniquely determined. In particular, for 2D structures such as 2D materials, patterned circuits, thin films or semiconductor electron and

hole gases, a spatial map of a single magnetic field component can be used to fully reconstruct the source current or out-of-plane magnetization distribution. Since some of the most interesting and elusive effects are observed over length scales of less than $1\ \mu\text{m}$ and with currents less than $1\ \mu\text{A}$ or magnetizations of few $\mu_{\text{B}}\ \text{nm}^{-2}$, techniques are required with both nanometre-scale spatial resolution and a sensitivity to fields smaller than $1\ \mu\text{T}$.

In SPM, high spatial resolution is achieved by minimizing both sensor size and its distance from the sample. High sensitivity is obtained by maximizing the signal-to-noise ratio for the magnetic signal of interest and the fundamental noise of the measurement. In evaluating the sensitivity of different techniques to magnetic contrast, we consider two idealized sources of magnetic field: a magnetic dipole moment and a line of current. This procedure²⁸ allows us to assess and compare the sensitivity of each technique to magnetization and current density in a sample (FIG. 2).

Magnetic force microscopy

Working principle and conditions. The most common technique for imaging magnetic fields of surfaces with high spatial resolution is MFM, which was introduced in the late 1980s as a natural extension of atomic force microscopy^{29,30}. The magnetostatic interaction between the stray magnetic fields of a sample and the magnetic tip of a mechanically compliant scanning probe creates the contrast in the image. The vibration frequency and amplitude of a cantilever probe, whose tip has been coated with a ferromagnetic film, are recorded as the probe is scanned above a sample. The response typically depends on a gradient of the stray field. Although some simplifying assumptions can often be made, extracting exact magnetic field maps from MFM images involves a deconvolution requiring knowledge of the shape and magnetization configuration of the tip.

MFM is possible under a wide variety of conditions, including in air, liquid, vacuum and over a broad range of temperatures. An MFM system consists of the cantilever, piezoelectric positioners for moving the sample and a set-up for detecting cantilever motion, usually by optical deflection or interferometry (FIG. 1a). Scan areas are typically in the range of a few micrometres by a few micrometres and take several minutes. The cantilever's mechanical frequency, typically a few hundred kHz, sets the upper limit on the speed of the dynamics that can be measured. In fact, measurement bandwidths are limited to tens of Hz, due to the linewidth of the mechanical resonance or the speed of the phase-locked loop used for determining the cantilever's frequency.

Cantilevers are typically made from Si, SiO_2 or Si_3N_4 , and their tips are coated with a magnetic film of Co or Ni. Because cantilevers are optimized to probe surfaces on the atomic scale, they are designed to have spring constants around $1\ \text{N m}^{-1}$, which is slightly smaller than the spring constant of an atomic bond at the surface of a solid. As a result, conventional MFM can have extremely high spatial resolution, down to $10\ \text{nm}$ (REFS^{31,32}) at cryogenic temperatures and in vacuum, but more typically from 30 to $100\ \text{nm}$. The cantilever's large spring constant, however, makes MFM responsive only

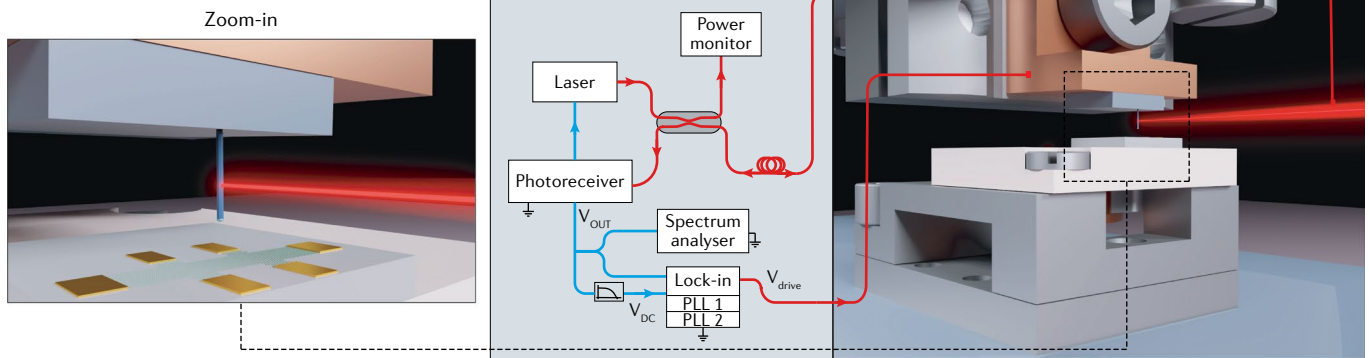
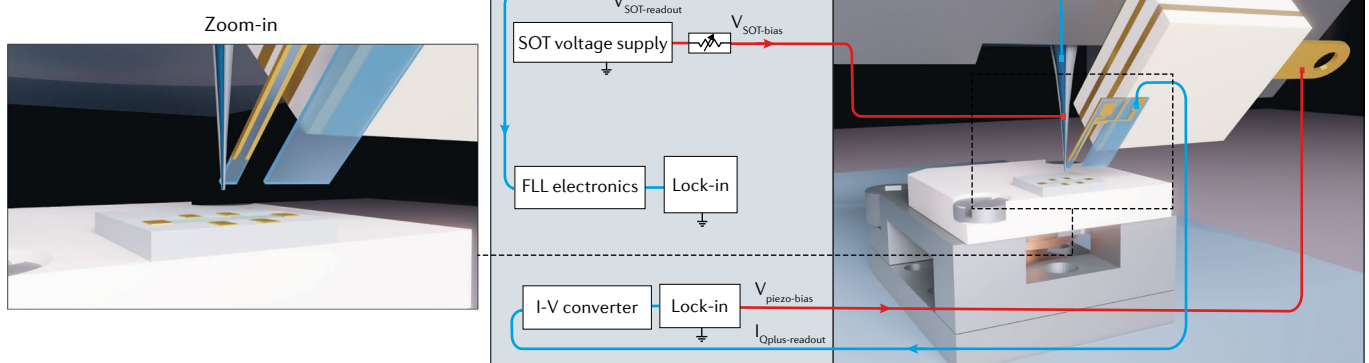
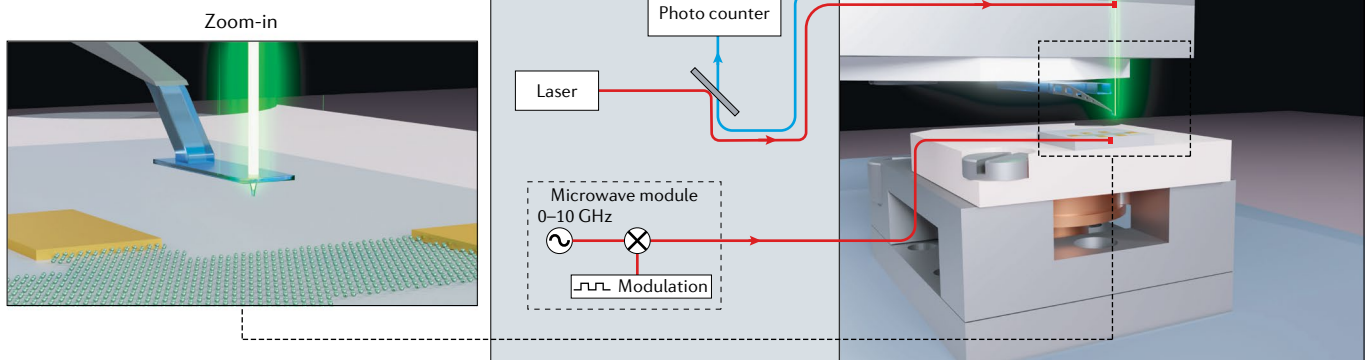
a Magnetic force microscopy

b Scanning SQUID microscopy

c Scanning NV microscopy


Fig. 1 | **Schematic diagrams for magnetic force microscopy, scanning SQUID microscopy and scanning NV microscopy.** Each diagram shows a sample mounted on a movable stage, actuated by piezoelectric positioners. For scale, the white sample holder in each diagram is 12×12 mm in lateral size. Above this sample is the scanning probe, along with its corresponding readout scheme. Insets show zoomed-in views of each probe, which more clearly depict the detection schemes. **a** | For nanowire magnetic force microscopy, focused laser light (red) is used for interferometric detection of the nanowire's flexural motion. **b** | For scanning superconducting quantum interference device (SQUID) microscopy, a mechanically coupled tuning fork is used for tip-sample distance control. **c** | For scanning nitrogen-vacancy (NV) microscopy, laser light (green) is used for NV excitation.

to strong magnetic field modulations on the order of tens of T ($\text{m Hz}^{1/2}$)⁻¹ (few μT over 100 nm measured in 1 s). Thus, MFM is well suited for the measurement of highly magnetized samples. However, it is ineffective for detecting the weak stray fields produced by subtle magnetization patterns or Biot–Savart fields of currents flowing through nanometre-scale devices.

The advent of cantilever probes consisting of individual nanowires^{33,34} or even carbon nanotubes³⁵ have

given researchers access to much smaller force transducers. This reduction in size led to both a better force sensitivity and a finer spatial resolution³⁶. Sensitivity to small forces provides the ability to detect weak magnetic fields and, therefore, to image subtle magnetic patterns; tiny concentrated magnetic tips have the potential to achieve nanometre-scale spatial resolution, while also reducing the invasiveness of the tip on the sample under investigation.

Nanowires have been demonstrated to maintain force sensitivities around $1 \text{ aN Hz}^{-1/2}$ near sample surfaces (within 100 nm) when operated in high vacuum and at cryogenic temperatures, due to extremely low non-contact friction³⁷. In recent proof-of-principle experiments, both magnet-tipped nanowires and fully magnetic nanowires were shown to be sensitive to magnetic field gradients of just a few mT $(\text{m Hz}^{1/2})^{-1}$ (REF.¹⁰) and a few nT $\text{Hz}^{-1/2}$ (REF.¹⁹), respectively. The latter are the gradients and fields produced by tens of $\mu_B \text{ Hz}^{-1/2}$, where μ_B is a Bohr magneton, or several nA $\text{Hz}^{-1/2}$ of flowing current, each at a distance of a hundred or so nanometres.

Sensitivity to different types of contrast. MFM can map either the magnetic field or magnetic field gradients. The ultimate noise limiting both these measurements is thermal noise acting on the transducer. Such noise causes random fluctuations in the measured vibration amplitude and frequency. Thermal noise sets a minimum measurable magnetic field or field gradient,

depending on the measurement type and the magnetization configuration of the tip (BOX 1). For example, a frequency shift measurement of a conventional MFM transducer³⁸ has a thermal limit at 4 K to static gradients of $(\frac{\partial B}{\partial r})_{\text{min}} \approx 30 \text{ T (m Hz}^{1/2})^{-1}$. Recently demonstrated nanowire MFM has a thermal limit for the same measurement that is about 1,000 times smaller³⁹.

By comparing the thermal noise background to the expected magnetic field or field gradient from a single Bohr magneton μ_B or a line or current I , we can assess the sensitivity of MFM (BOX 2). For example, conventional MFM scanning 50 nm above a sample is sensitive to frequency shifts equivalent to a magnetic moment of a few thousand $\mu_B \text{ Hz}^{-1/2}$ or currents of a few $\mu\text{A Hz}^{-1/2}$ (REF.³⁴). The same type of measurement carried out with newly demonstrated nanowire MFM probes 100 nm above a sample is about 100 times more sensitive to each type of contrast^{39,40}. The sensitivity to magnetic moment (FIG. 2a) and current (FIG. 2b) varies as a function of probe-sample spacing.

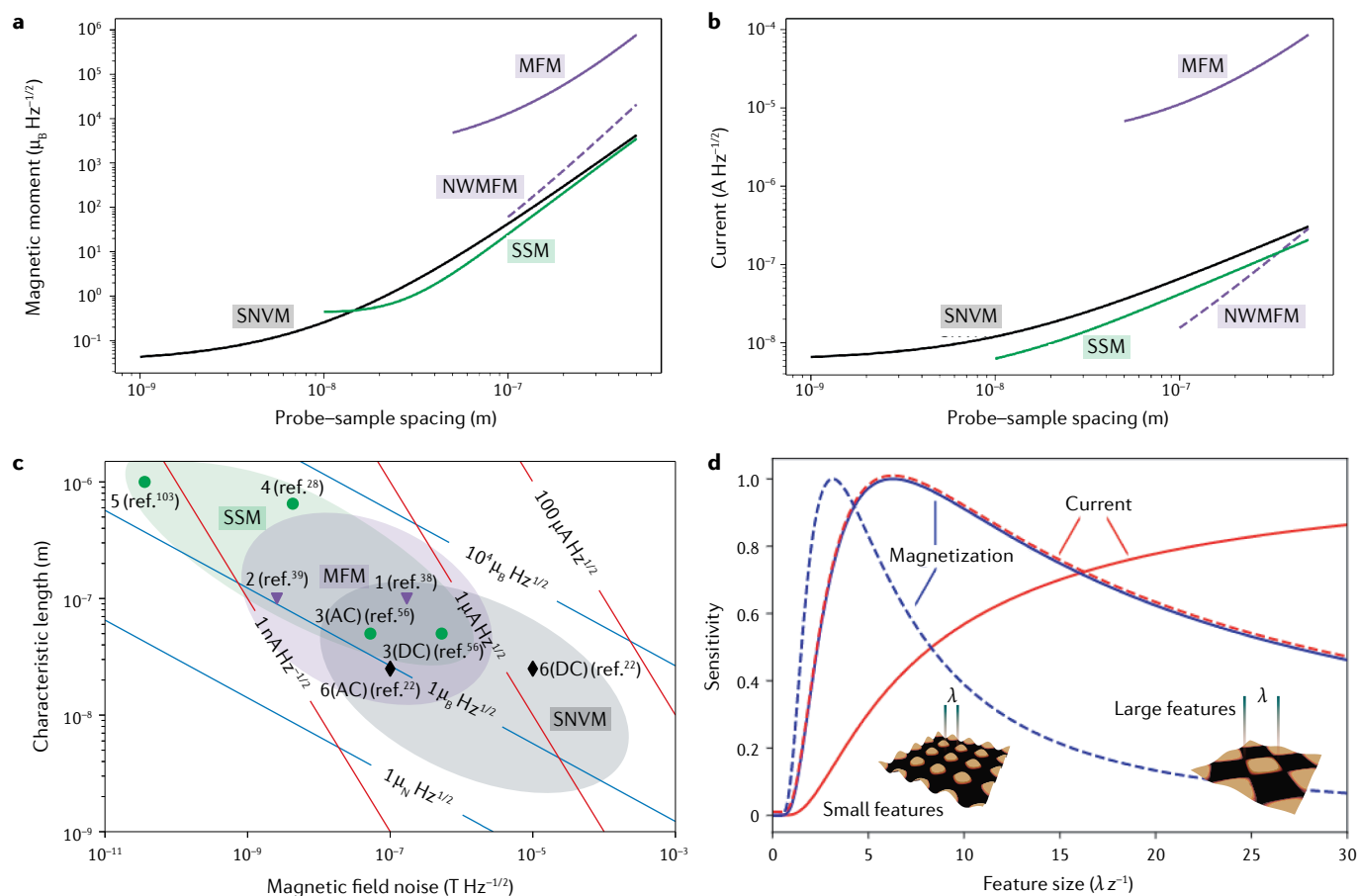


Fig. 2 | Comparing sensitivity and resolution of different magnetic imaging techniques. a,b | Sensitivity to magnetic moment and current of magnetic force microscopy (MFM), scanning superconducting quantum interference device (SQUID) microscopy (SSM) and scanning nitrogen-vacancy (NV) microscopy (SNVM). The sensitivities in panels **a** and **b** were taken in favourable conditions, under vacuum and at 4 K. MFM and nanowire MFM (NWMFM) sensitivities are based on frequency shift measurements at DC, while SNVM and SSM sensitivities are based on AC measurements, usually in the tens of kHz range. **c** | Characteristic length and magnetic field noise in favourable conditions, under vacuum and at 4 K. The characteristic

length sets the scale of the possible spatial resolution. Diagonal lines show the sensitivity required to measure the labelled magnetic moments and currents. **d** | Sensitivity as a function of feature size, expressed as the ratio between the feature's spatial wavelength λ and the probe-sample spacing z . Solid lines: magnetic field imaging is most sensitive to spatially large current features (red) and to magnetization features (blue) with a size similar to the probe-sample spacing z . Dashed lines: magnetic gradient imaging shifts the maximum sensitivity towards smaller feature size. Data for panels **a–c** taken with permission from REF.³⁸ for conventional MFM, REF.³⁹ for NWMFM, REFS.^{28,56,103} for SSM and REF.²² for SNVM.

Box 1 | Magnetic force microscopy

Force microscopy contrast is generated by the interaction of a cantilever tip with the sample underneath. By monitoring the vibration amplitude, one can measure tip–sample forces at the cantilever resonance frequency, while, by monitoring the vibration frequency, one can measure static tip–sample force gradients. The ultimate noise limiting these measurements is the thermal (Brownian) motion of the cantilever. Thermal noise sets a minimum measurable resonant force $F_{\min} = \sqrt{4k_{\text{B}}T\Gamma}$ in an amplitude measurement and a minimum measurable static force gradient $\left(\frac{\partial F}{\partial r}\right)_{\min} = \frac{1}{r_{\text{rms}}}\sqrt{4k_{\text{B}}T\Gamma}$ in a frequency measurement, where k_{B} is the Boltzmann constant, T is the temperature, Γ is the mechanical dissipation, r_{rms} is the cantilever oscillation amplitude and \hat{r} indicates the direction of cantilever oscillation.

In magnetic force microscopy, the magnetic tip transduces a magnetic field profile into a force profile. This interaction can often be approximated using a point-probe model, in which an effective magnetic multipole — including a monopole q and a dipole \mathbf{m} — represents the magnetization distribution of the tip. A magnetic field profile \mathbf{B} then produces a magnetic force acting on the cantilever given by $F_{\text{MFM}} = q\mathbf{B} \cdot \hat{r} + \nabla(\mathbf{m} \cdot \mathbf{B}) \cdot \hat{r}$. Note that, in most cases, the contribution of the torque generated by \mathbf{B} is negligible. For conventional magnetic force microscopy, where the tip–sample interaction can be approximated by a pure magnetic monopole, this results in a minimum measurable resonant magnetic field $B_{\min} = \frac{1}{q}\sqrt{4k_{\text{B}}T\Gamma}$ and a minimum measurable static magnetic field gradient $\left(\frac{\partial B}{\partial r}\right)_{\min} = \frac{1}{qr_{\text{rms}}}\sqrt{4k_{\text{B}}T\Gamma}$. Purely dipolar tips, such as those on the ends of some nanowires^{40,41}, are sensitive to a further spatial derivative of the magnetic field, compared with monopolar tips. Similar expressions can be written limiting those measurements.

It should be noted that the thermal limit on frequency measurements is rarely reached in practice. Most frequency measurements are limited by other noise sources, such as temperature variations, adsorption–desorption noise or other microscopic mechanisms intrinsic to the resonator, that are typically an order of magnitude larger⁴¹. However, measurements of resonant oscillation amplitude, which are sensitive to modulations at the mechanical frequency of the sensor (typically in the 100 kHz regime), are often thermally limited. In such measurements, conventional MFM cantilevers can be sensitive to a few hundred $\mu_{\text{B}} \text{ Hz}^{-1/2}$ or a few hundred nA $\text{Hz}^{-1/2}$, while nanowire MFM transducers reach down to a few $\mu_{\text{B}} \text{ Hz}^{-1/2}$ or a few nA $\text{Hz}^{-1/2}$.

Applications to 2D materials. Despite the lack of conventional MFM studies on 2D materials, researchers are starting to employ high-sensitivity MFM probes to visualize correlated states in 2D systems via maps of magnetic field or field gradient, which can, ultimately, be reconstructed in current density or magnetization contrast. Such images would be particularly useful for measuring the spatial localization of flowing currents, as in edge states, and for the determination of length scales such as magnetic domain sizes and coherence lengths. Visualizing current flow in magic-angle twisted bilayer graphene⁴² and WeT_2 (REFS^{43,44}), while they are electrostatically tuned into their superconducting states, could help to reveal the origin of this superconductivity and whether or not it is topological. Nanowire MFM may also help to provide direct evidence for magnetism in 2D magnets or even in the 2D semiconductor, monolayer MoS_2 (REFS^{45,46}). Optical spectroscopy has provided evidence of a high-field spin-polarized state in monolayer MoS_2 ; however, confirmation of its presence via a direct measurement of magnetic field has not yet been possible. Nanowire MFM's high sensitivity and ability to operate in high-field conditions make it promising for such an investigation.

MFM can also be used to map dissipation in a sample by measuring the power required to maintain a constant oscillation amplitude. This type of contrast maps the energy transfer between the tip and the sample, and provides excellent contrast for nanometre-scale magnetic structures⁴⁷. Since energy dissipation plays a central role in the breakdown of topological protection, it may provide important contrast in spatial studies of strongly correlated states in 2D vdW materials. Dissipation contrast has been used to observe superconducting⁴⁸ and bulk structural phase transitions⁴⁹, as well as the local density of states. 2D materials engineering allows for the fabrication of devices in which a variety of different physical phases can be accessed by the application of a gate voltage. Local measurements of dissipation via MFM could be an important tool for making spatial maps of the transitions between those states.

Scanning SQUID microscopy

Working principle and conditions. Taking advantage of a SQUID's extreme sensitivity to magnetic flux, SSM was first realized in the early 1980s⁵⁰. Contrast results from the magnetic flux threading through a superconducting loop that is interrupted by at least one Josephson junction. The SQUID's critical current is periodic in the flux through a superconducting loop — given by the magnetic field \mathbf{B} integrated over the area of the loop $\Phi_z = \int \mathbf{B} \cdot d\mathbf{A}$ — with a period given by the flux quantum Φ_0 . By applying the appropriate current bias, one can detect voltages across the SQUID that correspond to changes in magnetic field threading the SQUID loop corresponding to fractions of Φ_0 , typically down to $10^{-6} \Phi_0 \text{ Hz}^{-1/2}$. For imaging applications, a DC SQUID with two Josephson junctions is most often used. This loop — or a pickup loop inductively coupled to it — is scanned above a target sample in order to map the magnetic field profile. The loop's size is minimized in order to optimize spatial resolution. SQUIDs operate only below a superconducting transition temperature, which is typically below 10 K, but can be above the temperature of liquid nitrogen (77 K) for some high-temperature superconductors.

An SSM system consists of the SQUID sensor or pickup loop and piezoelectric positioners for moving the sample (FIG. 1b). In high-sensitivity and high-resolution applications, these elements are in a cryostat and in vacuum. Precise control of the sensor–sample distance can be achieved, for example, by coupling it to a micro-mechanical tuning fork^{51,52}. As in MFM, scan areas are in the micrometre range and take several minutes. The SQUID sets the system's ultimate bandwidth, which can be in the GHz range, but stray capacitance, cabling and detection electronics typically limit the bandwidth to tens of MHz or below.

As imaging resolution has improved from the micrometre-scale down into the nanometre-scale, a number of strategies have been employed to realize ever-smaller sensors, which simultaneously retain high magnetic flux sensitivity and can be scanned in close proximity to a sample. One strategy has involved miniaturizing the pickup loop of a conventional SQUID and placing it at the extreme corner of the chip, where it can

come close to a sample. The most advanced example of this design uses a loop with a 200-nm inner diameter to achieve sub-micrometre imaging resolution and a sensitivity of $130 \text{ nT Hz}^{-1/2}$ (REF.⁵³). Although this design

has the advantage of allowing for susceptibility measurements, the size of the sensor and minimum distance from the sample, which together determine the imaging resolution, are limited by the complex fabrication process. In the last decade, this limitation has been addressed through the development of SQUID-on-tip sensors, consisting of a SQUID fabricated by shadow evaporation or directional sputtering of a metallic superconductor directly on the end of a pulled quartz tip^{54,55}. This process has resulted in scanning SQUID sensors with diameters down to 50 nm, 100-nm imaging resolution and a sensitivity of $5 \text{ nT Hz}^{-1/2}$ (REF.⁵⁶).

Box 2 | Magnetic field sources

When comparing techniques, we consider two idealized sources of magnetic field, a magnetic dipole moment (see the figure, top panel) and a line of current (see the figure, bottom panel). The magnetic field of a magnetic moment \mathbf{m} at distance \mathbf{r} is given by $\mathbf{B}_m = \frac{\mu_0}{4\pi r^3} (3(\mathbf{m} \cdot \mathbf{r})\mathbf{r} - \mathbf{m})$ and the magnetic field of a line of current I is given by $\mathbf{B}_I = \frac{\mu_0 I \times \mathbf{r}}{2\pi r^2}$, where μ_0 is the vacuum permeability. Using these two equations, we can express the various quantities measured by our scanning probe sensors as a function of tip-sample spacing in terms of μ_B of magnetic moment or A of current. For example, for scanning nitrogen-vacancy centre microscopy measuring the z -component of the stray magnetic field, the maximum measurable signal from a single μ_B moment pointing along the z -direction at a tip-sample spacing z is $B_{\mu_B,z} = \frac{\mu_0 \mu_B}{2\pi z^3}$, while the maximum from a line of current I flowing in the plane is $B_{I,z} = \frac{\mu_0 I}{4\pi z}$. Similar expressions can be written for the maximum magnetic flux in the z -direction from the same moment and current measured by scanning superconducting quantum interference device (SQUID) microscopy.

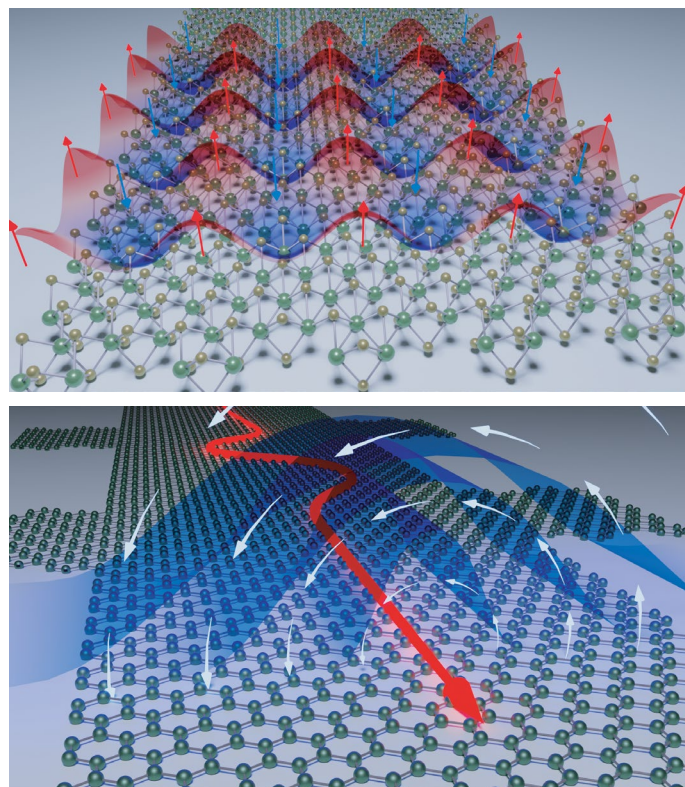
$$\Phi_{\mu_B,z} = \frac{\mu_0 \mu_B R^2}{2(z^2 + R^2)^{3/2}},$$

where R is the SQUID radius and

$$\Phi_{I,z} = \frac{\mu_0 I D}{4\pi} \ln \left(\frac{D^2 + 4z^2 + D\sqrt{D^2 + 4z^2}}{D^2 + 4z^2 - D\sqrt{D^2 + 4z^2}} \right),$$

where D is the length of one side of a square SQUID loop (to simplify the calculation, the current is integrated over a square rather than a circular loop). The corresponding maximum static magnetic field gradients measured by standard magnetic force microscopy are

$$\frac{\partial B_{\mu_B,z}}{\partial z} = \frac{3\mu_0 \mu_B}{2\pi z^4} \text{ and } \frac{\partial B_{I,z}}{\partial z} = \frac{3\sqrt{3}\mu_0 I}{16\pi z^2}.$$



Sensitivity to different types of contrast. The noise limiting the measurement of magnetic flux in a SQUID arises from several sources, including Johnson noise, shot noise, $1/f$ noise and quantum noise²⁸. For SQUIDs smaller than $1 \mu\text{m}$ and at frequencies high enough to avoid $1/f$ noise, quantum noise sets the fundamental limit on detectable flux to be $\Phi_Q = (\hbar L)^{1/2}$, where \hbar is Planck's constant and L is the loop inductance^{28,57,58}. State-of-the-art SQUID-on-tip sensors made from Pb combine the highest flux sensitivity with the smallest sensor size. In the white noise limit (measured in the kHz range), sensors with 50 nm diameter reach $\Phi_{\min} = 50 \text{ n}\Phi_0 \text{ Hz}^{-1/2}$, which is about four times larger than Φ_Q (REF.⁵⁶). Near DC (measured in the Hz range), where the same sensor is limited by $1/f$ noise, Φ_{\min} is about ten times larger. In these devices, L is dominated by kinetic rather than geometric inductance. For this reason, optimizing material parameters for low kinetic inductance provides the best route for improving Φ_{\min} .

Translating this sensitivity to magnetization or current sources requires knowing the tip-sample spacing. Using the best 50-nm-diameter SQUID-on-tip at a spacing of 50 nm — closer approach than the characteristic sensor size does not improve spatial resolution — the white noise level is equivalent to the field of a few $\mu_B \text{ Hz}^{-1/2}$ or a few tens of $\text{nA Hz}^{-1/2}$, while at DC, the device is ten times less sensitive (FIG. 2a,b).

Applications to 2D materials. SSM has already been successfully used to image current density via local measurements of Biot–Savart fields. In particular, maps of the flow of equilibrium currents in graphene made using SQUID-on-tip probes revealed the topological and non-topological components of edge currents in the quantum Hall state¹⁵ (FIG. 3a). The non-topological currents, which are of opposite polarity to the topological currents, were predicted theoretically⁵⁹, but are not typically considered because they do not affect conventional transport measurements⁶⁰. In fact, although previous SPM experiments, including Kelvin probe⁶¹, scanning single-electron transistor⁶² and scanning capacitance⁶³, revealed the presence of compressible and incompressible regions, non-topological currents were never observed. This new insight into the microscopic make-up of orbital currents in the quantum Hall systems was made possible by the SSM's sensitivity to tiny magnetic fields. Similar images of equilibrium currents in magic-angle twisted bilayer graphene (FIG. 3b) revealed the twist-angle disorder in these samples with

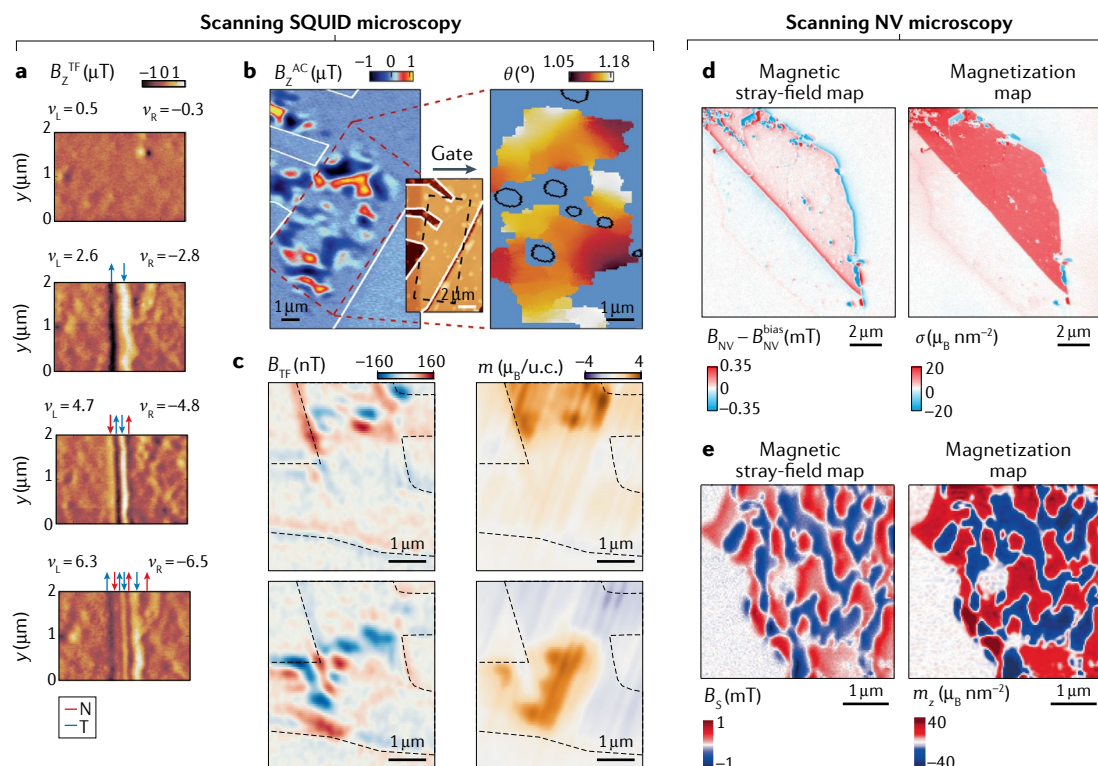


Fig. 3 | **Scanning probe microscopy measurements of magnetic field on 2D systems.** **a** | Maps of magnetic field gradient measured by scanning superconducting quantum interference device (SQUID) microscopy showing the flow of equilibrium currents in graphene at the interface between regions with different filling factors. The magnetic gradient image closely resembles the current density image, so that no reconstruction is needed. The images reveal the topological and non-topological components of edge currents in the quantum Hall state. **b** | Similar magnetic gradient image (left) of equilibrium currents in magic-angle twisted bilayer graphene and the corresponding map of twist angle (right) derived from it, revealing the twist-angle disorder in these samples. **c** | The difference in local magnetic field gradients (left) and the corresponding reconstructed 2D magnetization (right) in twisted bilayer graphene for different values of the Hall resistance measured by scanning SQUID microscopy. The images provide evidence for micrometre-scale domains of weak orbital magnetization in twisted bilayer graphene. **d** | Image of the stray magnetic field above a flake CrI_3 (left) measured by scanning nitrogen-vacancy (NV) microscopy and the corresponding magnetization map (right) derived from it, which shows evidence of layer-dependent magnetism. **e** | Image of the stray magnetic field above the 2D magnet CrBr_3 (left) and the corresponding magnetization map (right) showing domain walls pinned by defects. Panel **a** adapted from REF.¹⁵, Springer Nature Limited. Panel **b** adapted from REF.¹³, Springer Nature Limited. Panel **c** adapted with permission from REF.¹⁴, AAAS. Panel **d** adapted with permission from REF.¹⁷, AAAS. Panel **e** adapted from REF.¹⁸, CC BY 4.0.

a resolution and over an extent not possible by other techniques¹³. In those experiments, SSM also provided a direct correlation between the degree of disorder and the presence of correlated states, including superconductivity. In another set of measurements, SSM with the same kind of SQUID-on-tip sensor found evidence for orbital magnetism in twisted bilayer graphene¹⁴ (FIG. 3c). Images of the weak orbital magnetization and the presence of micrometre-scale domains, both of which have not been previously observed, were, once again, made possible by the technique's sensitivity to magnetic field combined with its spatial resolution.

Given the SQUID-on-tip's exquisite sensitivity to local temperature, such probes can also be applied to measure local sources of dissipation, as was demonstrated in experiments on graphene^{64,65}. Similar scanning probe measurements of magnetic field and dissipation could be carried out on other moiré systems, including twisted transition metal dichalcogenides and twisted multilayer graphene. These systems are also predicted

to host a variety of correlated states, including superconductivity, Mott insulating states, magnetic states and Wigner crystal states⁶⁶.

Scanning NV centre microscopy

Working principle and conditions. Following proposals in 2008 pointing out its potential for high-resolution, high-sensitivity magnetic field imaging^{67,68}, the last decade has seen a flurry of activity in the development of SNVM. In this scheme, NV centres, which are optically addressable electronic defect spins in diamond, are used as scanning single-spin sensors. Magnetic field measurements are carried out via optically detected magnetic resonance (ODMR) spectroscopy, where the electron paramagnetic resonance spectrum of the NV is recorded by simultaneous microwave excitation and optical read-out of the defect's spin state as the probe is scanned in close proximity to the sample surface. Thanks to the technique of single-molecule fluorescence, these experiments can be performed on a single spin⁶⁹. The magnetic

field sensitivity results from a Zeeman shift of the spin resonances. In the regime of a weak orthogonal component of an external magnetic field, the field component parallel to the NV symmetry axis leads to a linear shift of the $m_s = \pm 1$ spin states with a proportionality given by the free-electron gyromagnetic ratio $\gamma = 2\pi \times 28 \text{ GHz T}^{-1}$ (REF.⁷⁰). The ODMR spectrum is measured as a change in optical intensity as a function of continuous-wave or pulsed microwave excitation⁷¹. Other forms of contrast include ODMR quenching in magnetic fields larger than 10 mT due to energy-level mixing by the off-axis field component^{72,73} and spin relaxometry⁷⁴. The latter probes high-frequency fluctuations near the NV resonance (GHz range) and allows for the investigation of magnetic fluctuations and spin waves in ferromagnets^{75–77}. Further, dynamical decoupling techniques can be used to perform frequency spectroscopy in the kHz–MHz range^{78,79}.

In scanning probe applications, the NV centre is hosted within a crystalline diamond nanopillar and scanned over the sample of interest^{67,80} (FIG. 1c). State-of-the-art diamond probes are engineered with shallow NV centres, which are implanted at depths around 10 nm from the surface of the nanopillar⁸¹, in order to minimize the distance between the NV centre and the sample, and, thus, to optimize both sensitivity and spatial resolution. However, in most SNVM literature, the NV stand-off distance (the actual distance of the NV from the sample of interest) is 50–100 nm, indicating that NV centres may be deeper than expected. As in MFM and SSM, the sample is scanned below the probe, usually using piezoelectric positioners, while precise distance control is achieved by coupling to a micromechanical tuning fork. An objective lens above the probe is used to optically excite the NV centre and to detect its fluorescence.

Using advanced sensing protocols and sequences of microwave and laser pulses, scanning NV centre microscopes have achieved field sensitivities down to a few $\mu\text{T Hz}^{-1/2}$ (REF.⁸²) for DC signals and around $100 \text{ nT Hz}^{-1/2}$ (REF.²²) for AC signals. The best resolutions reported for scanning set-ups are between 15 and 25 nm (REFS^{74,83}), although resolution better than 10 nm should ultimately be possible for optimized scanning tips with very shallow NV centres. On top of high sensitivity and spatial resolution, scanning NV microscopy offers additional benefits: a large temperature range, including room temperature, a quantitative measurement of the magnetic field that is intrinsically calibrated via natural constants, vector sensitivity and a number of spin manipulation protocols for performing spectroscopy from DC to GHz signal frequencies.

These advantages notwithstanding, scanning NV microscopy remains challenging at high fields due to the high microwave frequencies (tens to hundreds of GHz) required to actuate the sensor electron spin, and the spin-level mixing for magnetic fields that are not aligned with the NV symmetry axis^{72,73}. Although NV centre detection has been reported below 1 K, experiments at cryogenic temperatures are hampered by reduced photoluminescence contrast and poor charge stability. Furthermore, the required optical and

microwave excitation sometimes poses a limit on the possible samples, since it can perturb materials such as direct-band-gap semiconductors, nanomagnets and fragile biological structures.

Sensitivity to different types of contrast. SNVM is typically limited by photon shot noise from the optical readout, and can be expressed by a simple signal-to-noise formula typical for optical magnetometry⁸⁴. Specifically, the magnetic sensitivity of the scanning NV magnetometer is determined by a combination of the spin dephasing or decoherence time (T_2), the optical contrast (ϵ) and the maximum photon count rate (I_0). A generic estimate for the minimum detectable magnetic field is given by $B_{\text{min}} \approx [\gamma \epsilon \sqrt{I_0 t_{\text{acq}} T_2}]^{-1}$, where γ is the gyromagnetic ratio and t_{acq} is the photon integration time. Using typical values ($\epsilon = 0.2$, $I_0 = 200 \text{ Kcs}^{-1}$, $t_{\text{acq}} = 300 \text{ ns}$, $T_2 = T_2^* = 1.5 \mu\text{s}$), the minimum detectable field is about $1 \mu\text{T Hz}^{-1/2}$ for pulsed operation and $10 \mu\text{T Hz}^{-1/2}$ for continuous-wave operation. Recent SNVM experiments have shown state-of-the-art pulsed sensitivity of $100 \text{ nT Hz}^{-1/2}$ (REF.²²). In the future, the sensitivity can be improved by extending T_2 using isotopically purified (free of ^{13}C) material⁸⁵ and AC magnetometry techniques⁸⁶, improving the contrast through alternative readout schemes⁸⁷ and improving the count rate by photonic shaping^{88,89}.

If we assume the best demonstrated pulsed sensitivity and a 25 nm NV–sample distance, SNVM is sensitive to $1 \mu\text{B Hz}^{-1/2}$ or a few tens of $\text{nA Hz}^{-1/2}$ (FIG. 2a,b).

Applications to 2D materials. SNVM has been applied to image magnetization in the 2D ferromagnets^{17–19} and current flow in graphene^{20,21,90} and layered semimetals²². Given SNVM's particularly high sensitivity to magnetic moment, the technique is particularly suited for mapping magnetism in vdW magnets to distinguish domain structure, quantify the strength of the magnetism and confirm its origin. The ability to distinguish the magnetism of single atomic layers, as first shown in CrI_3 (REF.¹⁷) and later in CrBr_3 (REF.¹⁸) (FIG. 3d) and CrTe_2 (REF.¹⁹), is crucial for investigating the effect of each layer in vdW heterostructures. The ability of SNVM to retain high sensitivity at room temperature and under ambient conditions makes it applicable to magnetic systems with potential practical application in spintronic devices. Sub-micrometre spatial resolution also distinguishes SNVM from optical techniques such as a Kerr effect^{23,91} and magnetic circular dichroism microscopy^{92,93}, allowing it to resolve, for example, domain walls pinned by defects¹⁸ (FIG. 3e). Moreover, its ability to quantitatively measure stray field allows the mapping of local 2D magnetization with a precision not possible via optical techniques. High-frequency sensing with SNVM⁹⁴ may also be useful for investigating magnonic excitations in 2D magnets.

Although current mapping at temperatures below 4 K, such as required for studies of superconductivity in 2D materials, is still challenging, SNVM is ideal for experiments across a broad and higher temperature range. In fact, researchers have used SNVM to map hydrodynamic flow in graphene²⁰ and WTe_2 (REF.²²), which is strongest at intermediate temperatures. The ability to measure current flow over a wide range of temperatures

allowed, in both of these systems, the observation of a crossover from diffusive to viscous electron transport. In WTe_2 , SNVM revealed an unexpected temperature dependence, indicating that strong electron–electron interactions are likely phonon-mediated. Similar studies could be carried out in a plethora of other 2D systems, in which viscous electron transport may dominate under certain conditions.

Comparison between techniques

A comparison of key figures of merit of the techniques discussed in this Technical Review is provided in TABLE 1.

Probe–sample spacing. Probe–sample spacing sets the spatial resolution of an SPM technique and, depending on the type of contrast, also strongly affects sensitivity. The sensitivity of all techniques to the magnetic field profile produced by a magnetic moment and a line of current as a function of probe–sample spacing is plotted in FIG. 2a,b. In the case of conventional and nanowire MFM, we refer to the thermal limit of frequency shift measurements, which applies to DC or low-frequency measurements. In the other two cases, we use the minimum flux and field noise achieved in these devices in AC measurements in the tens of kHz range.

MFM sensitivity is not shown closer than 50 nm and nanowire MFM is not shown closer than 100 nm, because the point-probe approximation breaks down at tip–sample spacings smaller than the tip size and non-contact friction starts to dominate the force noise⁹⁵. Also, at such close spacing, the stray field produced by the MFM tip at the sample is often invasive. SSM sensitivity is not shown closer than 10 nm, because sensors are difficult to operate closer without a catastrophic crash. Since SNVM can essentially be operated in contact with the sample, we plot its sensitivity down to 1 nm of probe–sample spacing.

Depending on the tip–sample spacing, either SNVM or SSM have the highest sensitivity to magnetic moment. SSM appears best for tip–sample distances larger than 25 nm, while SNVM is better for closer approach. Conventional MFM is the least sensitive, while nanowire MFM is competitive with the other techniques. While very promising, nanowire MFM tip size must be reduced from state-of-the-art diameters of 100 nm

in order for the technique to become competitive in high-spatial-resolution imaging of magnetic moment.

Among proven techniques, SSM is most sensitive to current. While conventional MFM is the least sensitive, nanowire MFM appears to surpass all techniques between 500 and 50 nm. Once again, for spatial resolutions better than 10 nm, SNVM appears to be the best choice.

Sensor size. The sensor size also affects the sensitivity to magnetic field. We plot a few state-of-the-art sensors of each type and give an approximate idea of each technique’s operating regime, using the characteristic length of each sensor (its size in one dimension), together with its sensitivity to magnetic field (FIG. 2c). The characteristic length of a sensor not only sets its ultimate spatial resolution but also sets the optimum probe–sample spacing, since closer approach is either impossible or does not improve sensitivity. Diagonal lines represent the combined probe–sample spacing and field noise required to achieve a certain sensitivity to magnetic moment or current.

SNVM has the smallest characteristic length, due to the atomic scale of the NV centre and the possibility to implant NVs with long coherence times just 10 nm from the surface of a scanning probe. This makes SNVM the technique of choice for spatial resolution under 25 nm and for the detection of small magnetizations. Because the magnetic field produced by a magnetic moment drops off with the inverse cube of the probe–sample distance, a small sensor able to work in close proximity to the sample is crucial for this type of contrast.

SSM has the highest field sensitivity, but this comes at the expense of large sensor size. While conventional MFM appears too insensitive to measure weak magnetization or current density, the increased force sensitivity of nanowire MFM makes it competitive with the other two techniques. In fact, for the measurement of currents, where spatial resolutions better than 100 nm are not required, SSM and nanowire MFM are the best techniques. Because Biot–Savart fields fall off only with the inverse power of the probe–sample spacing, a small sensor is not as important in current measurements as it is in magnetization measurements.

Table 1 | Parameters for state-of-the-art magnetic scanning probe microscopies combining the highest sensitivity with the highest resolution

	MFM (conventional) ^{31,32,38,102–104}	MFM (nanowire) ³⁹	SSM (susceptometer) ⁵³	SSM (SQUID-on-tip) ⁵⁶	SNVM ^{22,74,82,83}
Sensor size	10–100 nm	100 nm	0.5 μm	50 nm	<1 nm
Sensor stand-off	10–100 nm	50 nm	330 nm	25 nm	50 nm
Spatial resolution	10–100 nm	100 nm ^a	0.5 μm	100 nm	15–25 nm
DC sensitivity	10–100 $\mu\text{T Hz}^{-1/2}$	3 nT Hz ^{-1/2a}	660 nT Hz ^{-1/2}	50 nT Hz ^{-1/2}	4 $\mu\text{T Hz}^{-1/2}$
AC sensitivity	170 nT Hz ^{-1/2}	3 nT Hz ^{-1/2}	130 nT Hz ^{-1/2}	5 nT Hz ^{-1/2}	100 nT Hz ^{-1/2}
Operating field	<20 T	<10 T	<30 mT	<1.2 T	<hundreds of mT
Operating temperature	<500 K	<300 K	<9 K	<7 K	<600 K

MFM, magnetic force microscopy; SNVM, scanning nitrogen-vacancy microscopy; SQUID, superconducting quantum interference device; SSM, scanning SQUID microscopy. ^aRepresents estimates based on the properties of the sensors, which have not yet been experimentally confirmed.

Aside from their sensitivity and resolution, each technique has properties making it more or less advantageous for certain samples. The strongly magnetic tip of a magnetic force microscope can produce tens of mT of magnetic field on a sample 50 nm away. This field can, in turn, perturb the sample, potentially altering its state. SNVM requires the excitation of the probe with visible laser light. This optical excitation can perturb optically active samples below the probe. SSM is minimally invasive, as the stray fields due to the Meissner effect on an SSM probe are nearly negligible. SSM, however, is the most limited from the environmental point of view, functioning only at temperatures below the superconducting transition of the SQUID, typically below 10 K. Both MFM and SNVM function at a wide range of temperatures and pressures. SSM must also work below its critical field, which, for state-of-the-art SQUID-on-tips, can be as high as a few T. SNVM is also limited in field, in that the frequency of the microwaves used to address the NV centre scale linearly with field and become impractically high above 1 T.

Reconstruction of magnetization or current from field images

Since magnetic field microscopy techniques do not directly image the current or magnetization pattern, but, rather, their stray field, the question arises as to whether and how the former may be reconstructed from a stray-field map. The relation between stray field and current density is governed by the Biot–Savart law, which, using the concept of bound currents, can also be applied to magnetization.

Box 3 | Reconstruction of current density and magnetization from a magnetic field image

The current density $\mathbf{J}=(J_x, J_y)$ and in-plane magnetization M_z of a 2D sample can be conveniently reconstructed from a magnetic field image by expressing the Biot–Savart law in k -space. Assume that we image in a plane at distance z above the sample, then the magnetic stray field in k -space is given by

$$B_z(k_x, k_y, z) = ig(k, z) \left[\frac{k_y}{k} J_x(k_x, k_y) - \frac{k_x}{k} J_y(k_x, k_y) \right],$$

where $g(k, z) = \frac{1}{2} \mu_0 d e^{-kz}$ is a transfer function with $d \ll z$ being the film thickness, k_x and k_y are the k -vectors and $k = (k_x^2 + k_y^2)^{1/2}$. Similar expressions can be derived for B_x and B_y , as well as for $d \geq z$ (REFS^{83,105}).

To reconstruct the current density from a magnetic field map, the relation is inverted,

$$J_x(k_x, k_y) = - \frac{ik_y W B_z(k_x, k_y, z)}{kg(k, z)} \quad \text{and}$$

$$J_y(k_x, k_y) = - \frac{ik_x W B_z(k_x, k_y, z)}{kg(k, z)},$$

where W is a window function, whose cut-off wavelength is adjusted to suppress high-frequency noise. Different choices for the window function have been reported in the literature, including Hann and rectangular and Tikhonov-based windows. The cut-off wavelength is typically of order z . An expression for reconstructing \mathbf{J} from an arbitrary B -field component is given in REF.⁸³.

Similar expressions can be derived for reconstructing an out-of-plane magnetization M_z or to reconstruct magnetic gradient images. To reconstruct M_z , note that $\mathbf{J} = \nabla \times \mathbf{M}$, and, therefore, $B_z(k_x, k_y) = kg(k, z) M_z(k_x, k_y)$ for the forward problem and $M_z(k_x, k_y) = W B_z(k_x, k_y, z) / kg(z, k)$ for the reverse problem. To reconstruct a magnetic gradient image, the transfer function incurs an additional factor of k due to the derivative.

Work in the late 1980s^{92,93} established a framework to compute the stray fields of 2D current density $\mathbf{J}(x, y)$ and 2D magnetization patterns $\mathbf{M}(x, y)$, respectively. The same work also specified the conditions in which a reconstruction of \mathbf{J} and \mathbf{M} is possible. In particular, they showed that 3D current densities and magnetization patterns do not produce a unique magnetic stray field pattern and cannot, therefore, be determined by stray-field imaging. Further, even an arbitrary 2D magnetization pattern does not possess a unique stray field because the divergence-free part of \mathbf{M} does not generate an external stray field and is left arbitrary⁹⁶. A rigorous solution does, however, exist for 2D current densities $\mathbf{J}=(J_x, J_y, 0)$ and out-of-plane magnetized films $\mathbf{M}=(0, 0, M_z)$. This solution can be extended to thick films if the magnetization, or current density, is uniform through the thickness⁸³. As a consequence, magnetic field imaging is especially useful for analysing 2D systems and thin-film devices.

Magnetic field maps do not reproduce all current or magnetization features with the same sensitivity. Looking at the mechanics of the reconstruction, it becomes clear that features smaller than the probe-sample spacing z produce negligible magnetic field at the sensor location, because stray fields decay exponentially with distance from the surface (BOX 3). The decay length is given by $\lambda/2\pi$, where λ is the spatial wavelength of the current or magnetization feature (FIG. 3d). Interestingly, large features compared with the probe-sample spacing, large λ/z , produce a strong signal for currents, but not for magnetization.

Imaging magnetic field gradients rather than magnetic fields allows one to push the maximum sensitivity towards smaller feature size. Magnetic gradient detection is the standard mode for MFM but can also be implemented for SSM and SNVM by a mechanical oscillation of the sensor^{15,67}. Using lock-in techniques to demodulate the resulting signal can also substantially reduce noise through spectral filtering. Gradient detection is especially attractive for imaging currents, because the magnetic gradient image closely resembles the current density image, so that no reconstruction is needed¹⁵. For SNVM, gradient imaging is attractive because it upconverts DC signals to AC, where much more sensitive magnetometry protocols are available^{67,86}.

Prospects for improvement

Improving MFM sensitivity requires stronger magnetic tips or transducers with better force sensitivity. Up to an order of magnitude in force sensitivity could be gained by using optimized nanowire transducers. MFM cantilevers have recently been realized with spring constants in the hundreds of mN m^{-1} and mechanical quality factors above 10^6 , resulting in nearly 100 times more sensitivity than conventional transducers. In general, however, improving the sensitivity of a mechanical transducer is achieved by reducing its size⁹⁷, as in recent work on nanowire MFM. Another route to improve magnetic field sensitivity is to increase the magnetic moment and size of MFM tips. This gain, however, comes at the cost of reducing spatial resolution and increasing

the perturbative effect of the probes, which now produce larger stray fields at the sample.

The spatial resolution of the MFM could be improved by utilizing the sharpest possible magnetic tips. Extensive work has been done in this area in the context of conventional MFM, achieving spatial resolutions down to 10 nm (REFS^{7,8,98,99}). Such work could be extended to high-force-sensitivity nanowire MFM. Smaller tips, however, have reduced magnetic moment and, consequently, a worse sensitivity to magnetic field profiles. In order to maintain high sensitivity, in general, the reduction in tip size should be accompanied with a reduction in transducer size.

Improvements in SSM field sensitivity could come from a reduction in the SQUID inductance. Given that this quantity is dominated by kinetic inductance in state-of-the-art devices, optimizing the superconducting material from which the device is made could be a fruitful pursuit. Further reduction of the characteristic size of SSM probes is difficult to imagine. SQUID-on-tip probes have been fabricated with diameters just under 50 nm. Reducing this size further would make the device size similar to the thickness of the deposited

superconducting film, complicating much of the process on which the fabrication is based. SQUIDs with feature sizes of only a few nanometres have been fabricated in YBCO using a focused ion beam of He (REF¹⁰⁰), raising the possibility of devices that are an order of magnitude smaller and potentially work at liquid nitrogen temperature. Nevertheless, substantial work remains to be done before such devices can be integrated onto scanning probes.

In order to reduce the characteristic length scale of SNVM, a number of researchers have focused on simultaneously reducing the implantation depth of NV centres and maintaining their coherence properties. Implantation depths of less than 3 nm have been reported combined with greater than 10 μ s coherence times¹⁰¹, giving a perspective of better than 10 nm imaging resolution combined with sub-10 nT Hz^{-1/2} sensitivity. So far, however, most reported stand-off distances remain between 50 and 100 nm and the best magnetic field sensitivities at 100 nT Hz^{-1/2}, and significant work may be needed to reduce either figure of merit.

Published online 1 October 2021

- Freeman, M. R. & Choi, B. C. Advances in magnetic microscopy. *Science* **294**, 1484–1488 (2001).
- McCord, J. Progress in magnetic domain observation by advanced magneto-optical microscopy. *J. Phys. D* **48**, 333001 (2015).
- Rougemaille, N. & Schmid, A. K. Magnetic imaging with spin-polarized low-energy electron microscopy. *Eur. Phys. J.* **50**, 20101 (2010).
- Stoll, H. et al. Imaging spin dynamics on the nanoscale using X-Ray microscopy. *Front. Phys.* **3**, 26 (2015).
- Bonetti, S. X-ray imaging of spin currents and magnetisation dynamics at the nanoscale. *J. Phys. Condens. Matter* **29**, 133004 (2017).
- Fischer, P. Magnetic imaging with polarized soft X-rays. *J. Phys. D* **50**, 313002 (2017).
- Belova, L. M., Hellwig, O., Dobisz, E. & Dan Dahlberg, E. Rapid preparation of electron beam induced deposition co magnetic force microscopy tips with 10 Nm spatial resolution. *Rev. Sci. Instrum.* **83**, 093711 (2012).
- Jaafar, M. et al. Customized MFM probes based on magnetic nanorods. *Nanoscale* **12**, 10090–10097 (2020).
- Schnez, S. et al. Imaging localized states in graphene nanostructures. *Phys. Rev. B* **82**, 165445 (2010).
- Lee, K. et al. Ultrahigh-resolution scanning microwave impedance microscopy of moiré lattices and superstructures. *Sci. Adv.* **6**, eabd1919 (2020).
- Quang, T. L. et al. Scanning tunneling spectroscopy of van der Waals graphene/semiconductor interfaces: absence of Fermi level pinning. *2D Mater.* **4**, 035019 (2017).
- Woessner, A. et al. Highly confined low-loss plasmons in graphene–boron nitride heterostructures. *Nat. Mater.* **14**, 421–425 (2015).
- Uri, A. et al. Mapping the twist-angle disorder and Landau levels in magic-angle graphene. *Nature* **581**, 47–52 (2020).
- Tschirhart, C. L. et al. Imaging orbital ferromagnetism in a moiré Chern insulator. *Science* **372**, 1323–1327 (2021).
- Uri, A. et al. Nanoscale imaging of equilibrium quantum Hall edge currents and of the magnetic monopole response in graphene. *Nat. Phys.* **16**, 164–170 (2020).
- Aharon-Steinberg, A. et al. Long-range nontopological edge currents in charge-neutral graphene. *Nature* **593**, 528–534 (2021).
- Thiel, L. et al. Probing magnetism in 2D materials at the nanoscale with single-spin microscopy. *Science* **364**, 973–976 (2019).
- Sun, Q.-C. et al. Magnetic domains and domain wall pinning in two-dimensional ferromagnets revealed by nanoscale imaging. *Nat. Commun.* **12**, 1989 (2021).
- Fabre, F. et al. Characterization of room-temperature in-plane magnetization in thin flakes of CrTe2 with a single-spin magnetometer. *Phys. Rev. Mater.* **5**, 034008 (2021).
- Jenkins, A. et al. Imaging the breakdown of ohmic transport in graphene. Preprint at *arXiv* <https://arxiv.org/abs/2002.05065> (2020).
- Ku, M. J. H. et al. Imaging viscous flow of the Dirac fluid in graphene. *Nature* **583**, 537–541 (2020).
- Vool, U. et al. Imaging phonon-mediated hydrodynamic flow in WTe2 with cryogenic quantum magnetometry. Preprint at *arXiv* <https://arxiv.org/abs/2009.04477> (2020).
- Huang, B. et al. Layer-dependent ferromagnetism in a van der Waals crystal down to the monolayer limit. *Nature* **546**, 270–273 (2017).
- Chen, W. et al. Direct observation of van der Waals stacking-dependent interlayer magnetism. *Science* **366**, 983–987 (2019).
- Yang, M. et al. Creation of skyrmions in van der Waals ferromagnet Fe₃GeTe₂ on (Co/Pd)_n superlattice. *Sci. Adv.* **6**, eabb5157 (2020).
- Li, Q. et al. Patterning-induced ferromagnetism of Fe₃GeTe₂ van der Waals materials beyond room temperature. *Nano Lett.* **18**, 5974–5980 (2018).
- Huang, B. et al. Emergent phenomena and proximity effects in two-dimensional magnets and heterostructures. *Nat. Mater.* **19**, 1276–1289 (2020).
- Kirtley, J. R. Fundamental studies of superconductors using scanning magnetic imaging. *Rep. Prog. Phys.* **73**, 126501 (2010).
- Martin, Y. & Wickramasinghe, H. K. Magnetic imaging by “force microscopy” with 1000 Å resolution. *Appl. Phys. Lett.* **50**, 1455–1457 (1987).
- Saenz, J. J. et al. Observation of magnetic forces by the atomic force microscope. *J. Appl. Phys.* **62**, 4293–4295 (1987).
- Schmid, I. et al. Exchange bias and domain evolution at 10 nm scales. *Phys. Rev. Lett.* **105**, 197201 (2010).
- Moser, A. et al. High-resolution magnetic force microscopy study of high-density transitions in perpendicular recording media. *J. Magn. Magn. Mater.* **287**, 298–302 (2005).
- Rossi, N. et al. Vectorial scanning force microscopy using a nanowire sensor. *Nat. Nanotechnol.* **12**, 150–155 (2017).
- de Lépinay, L. M. et al. A universal and ultrasensitive vectorial nanomechanical sensor for imaging 2D force fields. *Nat. Nanotechnol.* **12**, 156–162 (2017).
- Siria, A. & Niguès, A. Electron beam detection of a nanotube scanning force microscope. *Sci. Rep.* **7**, 11595 (2017).
- Poggio, M. Nanomechanics: sensing from the bottom up. *Nat. Nanotechnol.* **8**, 482–483 (2013).
- Nichol, J. M., Hemesath, E. R., Lauhon, L. J. & Budakian, R. Nanomechanical detection of nuclear magnetic resonance using a silicon nanowire oscillator. *Phys. Rev. B* **85**, 054414 (2012).
- van Schendel, P. J. A., Hug, H. J., Stiefel, B., Martin, S. & Güntherodt, H.-J. A method for the calibration of magnetic force microscopy tips. *J. Appl. Phys.* **88**, 435–445 (2000).
- Mattiat, H. et al. Nanowire magnetic force sensors fabricated by focused-electron-beam-induced deposition. *Phys. Rev. Appl.* **13**, 044043 (2020).
- Rossi, N., Gross, B., Dirnberger, F., Bougeard, D. & Poggio, M. Magnetic force sensing using a self-assembled nanowire. *Nano Lett.* **19**, 930–936 (2019).
- Sansa, M. et al. Frequency fluctuations in silicon nanoresonators. *Nat. Nanotechnol.* **11**, 552–558 (2016).
- Cao, Y. et al. Unconventional superconductivity in magic-angle graphene superlattices. *Nature* **556**, 43–50 (2018).
- Fatemi, V. et al. Electrically tunable low-density superconductivity in a monolayer topological insulator. *Science* **362**, 926–929 (2018).
- Sajadi, E. et al. Gate-induced superconductivity in a monolayer topological insulator. *Science* **362**, 922–925 (2018).
- Roch, J. G. et al. Spin-polarized electrons in monolayer MoS₂. *Nat. Nanotechnol.* **14**, 432–436 (2019).
- Roch, J. G. et al. First-order magnetic phase transition of mobile electrons in monolayer MoS₂. *Phys. Rev. Lett.* **124**, 187602 (2020).
- Grütter, P., Liu, Y., LeBlanc, P. & Dürig, U. Magnetic dissipation force microscopy. *Appl. Phys. Lett.* **71**, 279–281 (1997).
- Kisiel, M. et al. Suppression of electronic friction on Nb films in the superconducting state. *Nat. Mater.* **10**, 119–122 (2011).
- Kisiel, M. et al. Noncontact atomic force microscope dissipation reveals a central peak of SrTiO₃ structural phase transition. *Phys. Rev. Lett.* **115**, 046101 (2015).
- Rogers, F. P. *A Device for Experimental Observation of Flux Vortices Trapped in Superconducting Thin Film*. Thesis, Massachusetts Inst. Technol. (1983).
- Finkler, A. et al. Scanning superconducting quantum interference device on a tip for magnetic imaging of nanoscale phenomena. *Rev. Sci. Instrum.* **83**, 073702 (2012).
- Ceccarelli, L. *Scanning Probe Microscopy with SQUID-on-tip Sensor*. Thesis, Univ. Basel (2020).
- Kirtley, J. R. et al. Scanning SQUID susceptometers with sub-micron spatial resolution. *Rev. Sci. Instrum.* **87**, 093702 (2016).
- Finkler, A. et al. Self-aligned nanoscale SQUID on a tip. *Nano Lett.* **10**, 1046–1049 (2010).
- Bagani, K. et al. Sputtered Mo₂Re₂C₄ SQUID-on-tip for high-field magnetic and thermal nanoimaging. *Phys. Rev. Appl.* **12**, 044062 (2019).

56. Vasyukov, D. et al. A scanning superconducting quantum interference device with single electron spin sensitivity. *Nat. Nanotechnol.* **8**, 639–644 (2013).
57. Tesche, C. D. & Clarke, J. dc SQUID: noise and optimization. *J. Low Temp. Phys.* **29**, 301–331 (1977).
58. Mitchell, M. W. & Alvarez, S. P. Colloquium: Quantum limits to the energy resolution of magnetic field sensors. *Rev. Mod. Phys.* **92**, 021001 (2020).
59. Geller, M. R. & Vignale, G. Currents in the compressible and incompressible regions of the two-dimensional electron gas. *Phys. Rev. B* **50**, 11714 (1994).
60. Cooper, N. R., Halperin, B. I. & Ruzin, I. M. Thermoelectric response of an interacting two-dimensional electron gas in a quantizing magnetic field. *Phys. Rev. B* **55**, 2344 (1997).
61. Weis, J. & von Klitzing, K. Metrology and microscopic picture of the integer quantum Hall effect. *Phil. Trans. R. Soc. A* **369**, 3954–3974 (2011).
62. Feldman, B. E., Krauss, B., Smet, J. H. & Yacoby, A. Unconventional sequence of fractional quantum Hall states in suspended graphene. *Science* **337**, 1196–1199 (2012).
63. Suddards, M. E., Baumgartner, A., Henini, M. & Mellor, C. J. Scanning capacitance imaging of compressible and incompressible quantum Hall effect edge strips. *New J. Phys.* **14**, 083015 (2012).
64. Halbertal, D. et al. Nanoscale thermal imaging of dissipation in quantum systems. *Nature* **539**, 407–410 (2016).
65. Halbertal, D. et al. Imaging resonant dissipation from individual atomic defects in graphene. *Science* **358**, 1303–1306 (2017).
66. Andrei, E. Y. et al. The marvels of moiré materials. *Nat. Rev. Mater.* **6**, 201–206 (2021).
67. Degen, C. L. Scanning magnetic field microscope with a diamond single-spin sensor. *Appl. Phys. Lett.* **92**, 243111 (2008).
68. Balasubramanian, G. et al. Nanoscale imaging magnetometry with diamond spins under ambient conditions. *Nature* **455**, 648–651 (2008).
69. Gruber, A. et al. Scanning confocal optical microscopy and magnetic resonance on single defect centers. *Science* **276**, 2012–2014 (1997).
70. Felton, S. et al. Hyperfine interaction in the ground state of the negatively charged nitrogen vacancy center in diamond. *Phys. Rev. B* **79**, 075203 (2009).
71. Schirhagl, R., Chang, K., Loretz, M. & Degen, C. L. Nitrogen-vacancy centers in diamond: nanoscale sensors for physics and biology. *Annu. Rev. Phys. Chem.* **65**, 83–105 (2014).
72. Epstein, R. J., Mendoza, F. M., Kato, Y. K. & Awschalom, D. D. Anisotropic interactions of a single spin and dark-spin spectroscopy in diamond. *Nat. Phys.* **1**, 94–98 (2005).
73. Tetienne, J.-P. et al. Magnetic-field-dependent photodynamics of single NV defects in diamond: an application to qualitative all-optical magnetic imaging. *New J. Phys.* **14**, 103033 (2012).
74. Ariyaratne, A., Bluvstein, D., Myers, B. A. & Jayich, A. C. B. Nanoscale electrical conductivity imaging using a nitrogen-vacancy center in diamond. *Nat. Commun.* **9**, 2406 (2018).
75. Wolfe, C. S. et al. Off-resonant manipulation of spins in diamond via precessing magnetization of a proximal ferromagnet. *Phys. Rev. B* **89**, 180406 (2014).
76. van der Sar, T., Casola, F., Walsworth, R. & Yacoby, A. Nanometre-scale probing of spin waves using single electron spins. *Nat. Commun.* **6**, 7886 (2015).
77. Bertelli, I. et al. Magnetic resonance imaging of spin-wave transport and interference in a magnetic insulator. *Sci. Adv.* **6**, eabd3556 (2020).
78. Alvarez, G. A. & Suter, D. Measuring the spectrum of colored noise by dynamical decoupling. *Phys. Rev. Lett.* **107**, 230501 (2011).
79. Degen, C. L., Reinhard, F. & Cappellaro, P. Quantum sensing. *Rev. Mod. Phys.* **89**, 035002 (2017).
80. Maletinsky, P. et al. A robust scanning diamond sensor for nanoscale imaging with single nitrogen-vacancy centres. *Nat. Nanotechnol.* **7**, 320–324 (2012).
81. Ofori-Okai, B. K. et al. Spin properties of very shallow nitrogen vacancy defects in diamond. *Phys. Rev. B* **86**, 081406 (2012).
82. Wornle, M. S. et al. Coexistence of Bloch and Néel walls in a collinear antiferromagnet. *Phys. Rev. B* **103**, 094426 (2021).
83. Chang, K., Eichler, A., Rhensius, J., Lorenzelli, L. & Degen, C. L. Nanoscale imaging of current density with a single-spin magnetometer. *Nano Lett.* **17**, 2567–2573 (2017).
84. Budker, D. & Romalis, M. Optical magnetometry. *Nat. Phys.* **3**, 227–234 (2007).
85. Balasubramanian, G. et al. Ultralong spin coherence time in isotopically engineered diamond. *Nat. Mater.* **8**, 383–387 (2009).
86. de Lange, G., Risté, D., Dobrovitski, V. V. & Hanson, R. Single-spin magnetometry with multipulse sensing sequences. *Phys. Rev. Lett.* **106**, 080802 (2011).
87. Hopper, D. A., Lauigan, J. D., Huang, T.-Y. & Bassett, L. C. Real-time charge initialization of diamond nitrogen-vacancy centers for enhanced spin readout. *Phys. Rev. Appl.* **13**, 024016 (2020).
88. Momenzadeh, S. A. et al. Nanoengineered diamond waveguide as a robust bright platform for nanomagnetoimetry using shallow nitrogen vacancy centers. *Nano Lett.* **15**, 165–169 (2015).
89. Wan, N. H. et al. Efficient extraction of light from a nitrogen-vacancy center in a diamond parabolic reflector. *Nano Lett.* **18**, 2787–2793 (2018).
90. Lee, M. et al. Mapping current profiles of point-contacted graphene devices using single-spin scanning magnetometer. *Appl. Phys. Lett.* **118**, 033101 (2021).
91. Gong, C. et al. Discovery of intrinsic ferromagnetism in two-dimensional van der Waals crystals. *Nature* **546**, 265–269 (2017).
92. Jiang, S., Li, L., Wang, Z., Mak, K. F. & Shan, J. Controlling magnetism in 2D CrI₃ by electrostatic doping. *Nat. Nanotechnol.* **13**, 549–553 (2018).
93. Fei, Z. et al. Two-dimensional itinerant ferromagnetism in atomically thin Fe₃GeTe₂. *Nat. Mater.* **17**, 778–782 (2018).
94. Du, C. et al. Control and local measurement of the spin chemical potential in a magnetic insulator. *Science* **357**, 195–198 (2017).
95. Stipe, B. C., Mamin, H. J., Stowe, T. D., Kenny, T. W. & Rugar, D. Noncontact friction and force fluctuations between closely spaced bodies. *Phys. Rev. Lett.* **87**, 096801 (2001).
96. Beardsley, I. A. Reconstruction of the magnetization in a thin film by a combination of Lorentz microscopy and external field measurements. *IEEE Trans. Magn.* **25**, 671–677 (1989).
97. Braakman, F. R. & Poggio, M. Force sensing with nanowire cantilevers. *Nanotechnology* **30**, 332001 (2019).
98. Koblishka, M. R., Hartmann, U. & Sulzbach, T. Improving the lateral resolution of the MFM technique to the 10nm range. *J. Magn. Magn. Mater.* **272–276**, 2138–2140 (2004).
99. Gao, L. et al. Focused ion beam milled CoPt magnetic force microscopy tips for high resolution domain images. *IEEE Trans. Magn.* **40**, 2194–2196 (2004).
100. Müller, B. et al. Josephson junctions and squids created by focused helium-ion-beam irradiation of YBa₂Cu₃O_{7-x}. *Phys. Rev. Appl.* **11**, 044082 (2019).
101. Sangtawesin, S. et al. Origins of diamond surface noise probed by correlating single-spin measurements with surface spectroscopy. *Phys. Rev. X* **9**, 031052 (2019).
102. Yamaoka, T. et al. Vacuum magnetic force microscopy at high temperatures: observation of permanent magnets. *Microsc. Today* **22**, 12–17 (2014).
103. Jeffery, M., Van Duzer, T., Kirtley, J. R. & Ketchen, M. B. Magnetic imaging of moat-guarded superconducting electronic circuits. *Appl. Phys. Lett.* **67**, 1769–1771 (1995).
104. Zhigao, S. et al. Visualization of electronic multiple ordering and its dynamics in high magnetic field: evidence of electronic multiple ordering crystals. *ACS Appl. Mater. Interfaces* **10**, 20136–20141 (2018).
105. Roth, B. J., Sepulveda, N. G. & Wikswo, J. P. Using a magnetometer to image a two-dimensional current distribution. *J. Appl. Phys.* **65**, 361–372 (1989).

Acknowledgements

We thank H.-J. Hug, J. Kirtley and A. Kleibert for insightful discussions. We acknowledge the support of the Canton Aargau and the Swiss National Science Foundation under project grant 200020-178863, via the Sinergia grant Nanoskyrmionics (grant no. CRSII5-171003) and via the NCCR Quantum Science and Technology (OSIT). C.L.D. acknowledges funding by the Swiss National Science Foundation under project grant 20020-175600, by the European Commission under grant no. 820394 ASTERIOS and by the European Research Council under grant 817720 IMAGINE.

Author contributions

All authors researched data for the article, carried out calculations and contributed substantially to discussion of the content. L.C. made the figures, with input from E.M., N.R., C.L.D. and M.P. M.P. wrote the text, with input from E.M., L.L. and C.L.D. All authors reviewed the manuscript before submission.

Competing interests

The authors declare no competing interests.

Peer review information

Nature Reviews Physics thanks Ruslan Prozorov and the other, anonymous, reviewer(s) for their contribution to the peer review of this work.

Publisher's note

Springer Nature remains neutral with regard to jurisdictional claims in published maps and institutional affiliations.

© Springer Nature Limited 2021